PHYSICAL REVIEW FLUIDS **4**, 114609 (2019)

Inverse energy cascade and vortical structure in the near-wall region of turbulent channel flow

Fujihiro Hamba*

Institute of Industrial Science, The University of Tokyo, Komaba, Meguro-ku, Tokyo 153-8505, Japan

(Received 17 June 2019; published 27 November 2019)

Analysis of the energy transfer in scale space, in addition to the energy transport in physical space, is useful for obtaining a better understanding of inhomogeneous turbulence. In this work, the energy transfer in scale space is examined using the direct numerical simulation data of turbulent channel flow. A direct cascade of the streamwise and wall-normal components of the turbulent energy is seen, whereas an inverse cascade of the spanwise component is observed near the wall. The inverse energy cascade implies that the production term of the subgrid-scale (SGS) energy is negative in the averaged sense. The conditional average of the velocity field associated with the negative production is evaluated to extract typical flow structures contributing to the inverse cascade. As a result, a long streamwise vortex around the reference point, as well as a short one in the upstream region, is observed, which is reminiscent of a series of slightly tilted streamwise vortices with alternate signs of vorticity near the wall. The isosurface of the negative production attached to the long vortex suggests that the grid-scale velocity of the long vortex is enhanced by the SGS motion under the influence of the short upstream vortex. The enstrophy equation is further examined to confirm that the SGS effect increases the rotation of the long vortex.

DOI: 10.1103/PhysRevFluids.4.114609

I. INTRODUCTION

The energy spectrum in wave-number space is commonly used to describe the scale dependence of turbulent fluctuations in homogeneous isotropic turbulence. The energy cascade from low to high wave numbers has been studied in detail, and several closure theories have been proposed [1]. By contrast, for inhomogeneous turbulence, one-point statistical quantities such as the turbulent kinetic energy are employed. The energy production, dissipation, and transfer in physical space are typically investigated, and one-point closure models have been developed [2]. In order to obtain a better understanding of inhomogeneous turbulence, it is also useful to examine the energy transfer in scale space. If the velocity field in inhomogeneous turbulence is statistically homogeneous in several directions, the Fourier transform can be applied in those directions. For example, turbulent channel flows have been examined using the energy spectrum in the streamwise and spanwise directions [3–7]. Mizuno [6] evaluated the spectral energy budget equation to reveal the scale dependence of the energy transport. Lee and Moser [7] studied the scale dependence of the dynamics of the Reynolds stress by examining its transport equation.

It is meaningful to study the scale dependence of turbulent flows not only in homogeneous directions but also in inhomogeneous directions. Instead of the energy spectrum, the second-order velocity structure function $\langle \delta u_i^2(\mathbf{x},\mathbf{r})\rangle$ [where $\delta u_i(\mathbf{x},\mathbf{r}) = u_i'(\mathbf{x}+\mathbf{r}) - u_i'(\mathbf{x})$ and $u_i'(\mathbf{x})$ is the velocity fluctuation] and the two-point velocity correlation $Q_{ii}(\mathbf{x},\mathbf{r})\,[=\langle u_i'(\mathbf{x})u_i'(\mathbf{x}+\mathbf{r})\rangle]$ can be used to

---

*hamba@iis.u-tokyo.ac.jp

approximate the kinetic energy of eddies of length scale r $(=|\mathbf{r}|)$ in physical space. For homogeneous isotropic turbulence, the von Kármán–Howarth equation and the Kolmogorov equation were formulated using the two-point correlation and the structure function, respectively [1]. Several attempts have been made to extend these equations to inhomogeneous turbulence [8–17]. Danaila *et al.* [12] developed a scale-by-scale kinetic energy budget equation for inhomogeneous and anisotropic turbulence using the structure function. They examined experimental data obtained in a multiple-opposed-jet flow to validate the energy equation and clarify the anisotropic energy transfer. Using the generalized Kolmogorov equation, Cimarelli *et al.* [13,15] examined the energy flux occurring in scale space and physical space in turbulent channel flows. An interesting behavior of the energy flux was observed in which the inverse energy cascade plays a central role. Mollicone *et al.* [16] used the generalized Kolmogorov equation to examine the scale-by-scale dynamics in the separated turbulent flow behind a bump.

Using the two-point velocity correlation, the author proposed the energy density in scale space [14,17]. The energy density and its transport equation in scale space were investigated using the direct numerical simulation (DNS) data of turbulent channel flow. Profiles of the energy transfer term showed that a direct energy cascade from large to small scales was seen in most regions, whereas an inverse energy cascade from small to large scales was observed in a small region near the wall. The inverse energy cascade corresponds to energy transfer from the subgrid-scale (SGS) component to the grid-scale (GS) component. It is interesting to further investigate the behavior of the inverse cascade because it should be closely related to the process that sustains the GS turbulent motion, including coherent structures near the wall.

Coherent structures near the wall in wall-bounded flows have been studied in detail experimentally and numerically [18–27]. Hairpin vortices are simple coherent structures that explain several features of wall turbulence. Not only symmetric hairpins but also asymmetric ones have commonly been observed [18]. In the buffer layer, the legs of the hairpin become quasistreamwise vortices that push low-momentum fluid upward; this is called the ejection event. In the outer layer of the boundary layer, hairpin vortices occur in streamwise-aligned packets that propagate at nearly the same speed [20]. Large-scale motion on the order of the boundary layer thickness has also been observed in turbulent boundary layers and channel flows. In addition, very large-scale motion in a pipe flow was studied by experimental and DNS works [19,25]. These structures contribute considerably to the turbulent kinetic energy and Reynolds stress and they produce large-scale structures in the velocity fluctuations in the near-wall region [21,25,26,28].

Such coherent structures are observed in snapshots of fluid motion. We can identify some typical vortical structures from an instantaneous velocity field and examine them in detail. However, it is not necessarily clear whether such individual structures observed in a snapshot are universal. The conditional average of the flow field is then useful for determining the mean vortical structure around a reference point at which the flow makes strong contributions to some events [22,29–31]. For example, the conditionally averaged flow field associated with an ejection event near the wall was obtained using the DNS data of channel flow [22,29,32]. In order to investigate the influence of large-scale motion on the friction drag, Hwang and Sung [30] evaluated the near-wall vortical structures conditioned on the large-scale events using the DNS data of the turbulent boundary layer. Using particle image velocimetry experiments, de Silva *et al.* [31] evaluated conditionally averaged maps of the kinetic energy deficit near the turbulent bulges to investigate the large coherence of the spanwise velocity in turbulent boundary layers.

It is also important to investigate the mechanisms that generate and maintain coherent structures [33]. For example, Waleffe [34] proposed a self-sustaining process of the streamwise vortices. The process consists of three phases: The streamwise vortices create a streak structure with the aid of the mean shear, the instability of the streak structure generates three-dimensional velocity fluctuations, and the nonlinear effects of the three-dimensional fluctuations reenergize the streamwise vortices. This process is interesting as a candidate for the self-sustaining mechanism of wall turbulence. Nevertheless, further verification is necessary, because this process was proposed on the basis of a low-order model of the truncated system rather than on the exact Navier-Stokes equation. In terms of the energy transfer, the first and second phases correspond to a direct energy cascade from the mean to the fluctuating components, whereas the third one corresponds to an inverse energy cascade from the fluctuating to the mean components. Therefore, it is expected that flow structures related to the energy cascade will provide some insight into the self-sustaining process near the wall in real turbulent flows. In this study, we focus on the inverse energy cascade seen near the wall in turbulent channel flow. We use the conditional average of the velocity field associated with the inverse cascade, or the negative production of the SGS energy, to extract typical flow structures. We examine the relationship between the flow structures and the process of reenergizing the streamwise vortices.

This paper is organized as follows. In Sec. II we describe the transport equation for the energy density in scale space and evaluate the energy transfer near the wall in turbulent channel flow. In Sec. III we focus on the production term of the SGS energy to examine flow structures contributing to the inverse energy cascade. In Sec. IV we evaluate the conditional average of the velocity field associated with the negative production to extract typical flow structures and investigate the relationship between vortical structures and the inverse cascade. We summarize this paper in Sec. V.

II. ENERGY TRANSFER IN SCALE SPACE

In order to examine the interscale energy transfer in turbulent channel flow, we introduce the energy density and its transport equation in scale space [17]. The two-point velocity correlation separated in the streamwise (x) direction is defined as

$$Q_{ij}(\mathbf{x}, r_x) = \langle u_i'(\mathbf{x}) u_j'(\mathbf{x} + r_x \mathbf{e}_x) \rangle, \tag{1}$$

where $\langle \cdot \rangle$ is the ensemble average, u_i' $(= u_i - \langle u_i \rangle)$ is the velocity fluctuation, and $\mathbf{e}_x$ is the unit vector in the x direction. Using the correlation $Q_{ij}(\mathbf{x}, r_x)$, we can define the density of the Reynolds stress in scale space in the x direction as

$$R_{ij}(\mathbf{x}, r_x) = -\frac{\partial}{\partial r_x} R_{ij}^{>}(\mathbf{x}, r_x), \tag{2}$$

where

$$R_{ij}^{>}(\mathbf{x}, r_x) = \int_{-\infty}^{\infty} d\xi_x Q_{ij}(\mathbf{x}, \xi_x) G(\xi_x, r_x), \quad G(\xi, r) = \frac{1}{\sqrt{2\pi} r} \exp\left(-\frac{\xi^2}{2r^2}\right). \tag{3}$$

Hereafter, we treat the density of the normal stresses $R_{xx}(\mathbf{x}, r_x)$, $R_{yy}(\mathbf{x}, r_x)$, and $R_{zz}(\mathbf{x}, r_x)$ as well as that of the turbulent energy $E(\mathbf{x}, r_x)$ $[= R_{ii}(\mathbf{x}, r_x)/2]$ (summation convention is adopted for repeated indices of i, j, and k); they are called the energy density in this paper. The energy density $R_{ij}(\mathbf{x}, r_x)$ defined in Eq. (2) can also be written as

$$R_{ij}(\mathbf{x}, r_x) = \int_{-\infty}^{\infty} d\xi_x Q_{ij}(\mathbf{x}, \xi_x) G_D(\xi_x, r_x), \quad G_D(\xi, r) = \frac{1}{\sqrt{2\pi} r^2}\left(1 - \frac{\xi^2}{r^2}\right) \exp\left(-\frac{\xi^2}{2r^2}\right) \tag{4}$$

and satisfies the properties

$$\langle u_i' u_j' \rangle = \int_0^{\infty} dr_x R_{ij}(\mathbf{x}, r_x), \tag{5}$$

$$R_{\alpha\alpha}(\mathbf{x}, r_x) \geqslant 0, \tag{6}$$

where the summation is not taken for α. The property (6) holds in cases where the turbulent field is statistically homogeneous in the x direction.

The function $R_{ij}^{>}(\mathbf{x}, r_x)$ appearing in Eq. (3) represents the energy of eddies with sizes equal to or greater than the length scale r_x. The energy density $R_{ij}(\mathbf{x}, r_x)$ obtained from differentiation of $R_{ij}^{>}(\mathbf{x}, r_x)$ with respect to r_x represents the energy of eddies with sizes equal to the length scale r_x. In order to clarify the physical meaning of $R^{>}_{ij}(\mathbf{x}, r_x)$, we consider the filtered velocity commonly used in the large-eddy simulation as

$$\bar{u}_i(\mathbf{x}) = \int_{-\infty}^{\infty} dx' u_i(\mathbf{x} + x'\mathbf{e}_x) G_F(x', \Delta_x), \tag{7}$$

where $G_F(x, \Delta)$ is a filter function given by

$$G_F(x, \Delta) = \frac{\sqrt{6}}{\sqrt{\pi}\Delta} \exp\left(-\frac{6x^2}{\Delta^2}\right). \tag{8}$$

When the separation ξ_x appearing in Eq. (3) is taken in a statistically homogeneous direction, we can obtain the relationship [17]

$$R^{>}_{ij}(\mathbf{x}, r_x) = \langle \bar{u}'_i(\mathbf{x}) \bar{u}'_j(\mathbf{x}) \rangle, \tag{9}$$

where $\Delta_x = \sqrt{6} r_x$. Therefore, the function $R^{>}_{\alpha\alpha}(\mathbf{x}, r_x)$ is equivalent to the GS turbulent energy $\langle \bar{u}'^2_\alpha \rangle$. Applying a Gaussian filter to the DNS velocity field of the turbulent boundary layer, Motoori and Goto [35] investigated the generation mechanism of the hierarchy of multiscale vortices. The analysis of the energy density $R_{ij}(\mathbf{x}, r_x)$ is closely related to a similar analysis in which a filter is applied to the DNS field.

From the Navier-Stokes equation for $u'_i(\mathbf{x})$ and $u'_j(\mathbf{x} + \boldsymbol{\xi})$ ($\boldsymbol{\xi} = r_x \mathbf{e}_x$), we obtain the transport equation for $Q_{ij}(\mathbf{x}, r_x)$. Applying the integral appearing in Eq. (4) to each term in the equation, we can obtain the transport equation for $R_{ij}(\mathbf{x}, r_x)$ as [17]

$$\begin{aligned} \frac{D}{Dt} R_{ij}(\mathbf{x}, r_x) = {} & P_{ij}(\mathbf{x}, r_x) - \varepsilon_{ij}(\mathbf{x}, r_x) + \Pi_{ij}(\mathbf{x}, r_x) + D_{Tij}(\mathbf{x}, r_x) + D_{Pij}(\mathbf{x}, r_x) \\ & + D_{Vij}(\mathbf{x}, r_x) + T_{ij}(\mathbf{x}, r_x), \end{aligned} \tag{10}$$

where $D/Dt = \partial/\partial t + U_i \partial/\partial x_i$. The right-hand side consists of seven terms: the production $P_{ij}(\mathbf{x}, r_x)$, dissipation $\varepsilon_{ij}(\mathbf{x}, r_x)$, pressure strain $\Pi_{ij}(\mathbf{x}, r_x)$, turbulent diffusion $D_{Tij}(\mathbf{x}, r_x)$, pressure diffusion $D_{Pij}(\mathbf{x}, r_x)$, viscous diffusion $D_{Vij}(\mathbf{x}, r_x)$, and interscale transfer $T_{ij}(\mathbf{x}, r_x)$. They are defined as

$$\begin{aligned} P_{ij}(\mathbf{x}, r_x) = {} & - \int_{-\infty}^{\infty} d\xi_x G_D(\xi_x, r_x) \langle u'_k(\mathbf{x}) u'_j(\mathbf{x} + \boldsymbol{\xi}) \rangle \frac{\partial}{\partial x_k} U_i(\mathbf{x}) \\ & - \int_{-\infty}^{\infty} d\xi_x G_D(\xi_x, r_x) \langle u'_k(\mathbf{x} + \boldsymbol{\xi}) u'_i(\mathbf{x}) \rangle \frac{\partial}{\partial x_k} U_j(\mathbf{x} + \boldsymbol{\xi}), \end{aligned} \tag{11}$$

$$\varepsilon_{ij}(\mathbf{x}, r_x) = \int_{-\infty}^{\infty} d\xi_x G_D(\xi_x, r_x) \nu \left\langle s'_{ki}(\mathbf{x}) \frac{\partial}{\partial x_k} u'_j(\mathbf{x} + \boldsymbol{\xi}) + s'_{kj}(\mathbf{x} + \boldsymbol{\xi}) \frac{\partial}{\partial x_k} u'_i(\mathbf{x}) \right\rangle, \tag{12}$$

$$\Pi_{ij}(\mathbf{x}, r_x) = \int_{-\infty}^{\infty} d\xi_x G_D(\xi_x, r_x) \left\langle p'(\mathbf{x}) \frac{\partial}{\partial x_i} u'_j(\mathbf{x} + \boldsymbol{\xi}) + p'(\mathbf{x} + \boldsymbol{\xi}) \frac{\partial}{\partial x_j} u'_i(\mathbf{x}) \right\rangle, \tag{13}$$

$$D_{Tij}(\mathbf{x}, r_x) = -\frac{\partial}{\partial x_k} \int_{-\infty}^{\infty} d\xi_x G_D(\xi_x, r_x) \langle u'_k(\mathbf{x}) u'_i(\mathbf{x}) u'_j(\mathbf{x} + \boldsymbol{\xi}) \rangle, \tag{14}$$

$$D_{Pij}(\mathbf{x}, r_x) = -\frac{\partial}{\partial x_k} \int_{-\infty}^{\infty} d\xi_x G_D(\xi_x, r_x) [\langle p'(\mathbf{x}) u'_j(\mathbf{x} + \boldsymbol{\xi}) \rangle \delta_{ki} + \langle p'(\mathbf{x} + \boldsymbol{\xi}) u'_i(\mathbf{x}) \rangle \delta_{kj}], \tag{15}$$

$$D_{Vij}(\mathbf{x}, r_x) = \frac{\partial}{\partial x_k} \int_{-\infty}^{\infty} d\xi_x G_D(\xi_x, r_x) \nu \langle s'_{ki}(\mathbf{x}) u'_j(\mathbf{x} + \boldsymbol{\xi}) + s'_{kj}(\mathbf{x} + \boldsymbol{\xi}) u'_i(\mathbf{x}) \rangle, \tag{16}$$

$$T_{ij}(\mathbf{x}, r_x) = -\frac{\partial}{\partial r_x} \Pi_{Sij}(\mathbf{x}, r_x), \tag{17}$$

respectively, where

$$s'_{ij}(\mathbf{x}) = \frac{\partial}{\partial x_i}u'_j(\mathbf{x}) + \frac{\partial}{\partial x_j}u'_i(\mathbf{x}), \tag{18}$$

$$\begin{aligned}\Pi_{Sij}(\mathbf{x}, r_x) = & -\int_{-\infty}^{\infty} d\xi_x G(\xi_x, r_x)\frac{\partial}{\partial \xi_k}\langle[u'_k(\mathbf{x}+\boldsymbol{\xi}) - u'_k(\mathbf{x})]u'_i(\mathbf{x})u'_j(\mathbf{x}+\boldsymbol{\xi})\rangle \\ & -\int_{-\infty}^{\infty} d\xi_x G(\xi_x, r_x)\frac{\partial}{\partial \xi_k}\{[U_k(\mathbf{x}+\boldsymbol{\xi}) - U_k(\mathbf{x})]\langle u'_i(\mathbf{x})u'_j(\mathbf{x}+\boldsymbol{\xi})\rangle\}.\end{aligned} \tag{19}$$

The interscale transfer term $T_{ij}(\mathbf{x}, r_x)$ is written in the gradient form in Eq. (17) and $\Pi_{Sij}(\mathbf{x}, r_x)$ represents the energy flux in scale space. A negative value of $\Pi_{Sij}(\mathbf{x}, r_x)$ represents energy flux from large to small scales corresponding to a direct energy cascade. When each term in Eq. (10) is integrated from $r_x = 0$ to ∞, Eq. (10) reduces to the transport equation for the Reynolds stress $\langle u'_i u'_j\rangle$ in physical space. The first six terms on the right-hand side of Eq. (10) have corresponding terms in the Reynolds stress equation; the terms represent the scale dependence of physical processes such as production and dissipation. By contrast, the transfer term disappears in the Reynolds stress equation because

$$\int_0^{\infty} dr_x T_{ij}(\mathbf{x}, r_x) = 0. \tag{20}$$

Using the DNS data of turbulent channel flow, we examine the energy transfer in scale space described by Eq. (10). The DNS is carried out as follows. The size of the computational domain is $L_x \times L_y \times L_z = 2\pi \times 2 \times \pi$, where x, y, and z denote the streamwise, wall-normal, and spanwise directions, respectively. The number of grid points is $N_x \times N_y \times N_z = 1024 \times 192 \times 1024$. The Reynolds number based on the friction velocity u_τ and the channel half-width $L_y/2$ is set to $\mathrm{Re}_\tau = 590$. Hereafter, physical quantities are nondimensionalized by u_τ and $L_y/2$. Periodic boundary conditions are used in the streamwise and spanwise directions, and no-slip conditions are imposed at the wall at $y = 0, 2$. We use the fourth-order finite-difference scheme in the x and z directions, the second-order one in the y direction, and the Adams-Bashforth method for time marching. Statistical quantities such as the energy density were obtained by ensemble averaging (denoted by angular brackets) over the x-z plane and over the time period of $70 \leqslant t \leqslant 100$ normalized by $(L_y/2)/u_\tau$. As a result, the averaged quantities depend only on y and r_x. In our previous work [17] we investigated the energy transport in the whole domain of channel flow. Because simulation and analysis of flows at higher Reynolds number require very large computational cost, we choose a moderate Reynolds number $\mathrm{Re}_\tau = 590$. The Reynolds number is high enough for the present work where we focus on the near-wall structures.

Figure 1 shows the contours of the energy fluxes $\Pi_{Sxx}(y, r_x)$, $\Pi_{Syy}(y, r_x)$, $\Pi_{Szz}(y, r_x)$, and $\Pi_S(y, r_x)\,[= \Pi_{Sii}(y, r_x)/2]$ given by Eq. (19) in the r_x-y plane. The location at $y = 0$ corresponds to the bottom wall. Only the domain $0 \leqslant y^+ \; (=u_\tau y/\nu) \leqslant 300 \; (0 \leqslant y \leqslant 0.51)$ is shown to examine the near-wall region in detail. Contours of positive (negative) values are plotted as solid (dashed) lines. In Figs. 1(a), 1(b) and 1(d), contours with negative values are seen, indicating that a direct energy cascade from large to small scales occurs for $R_{xx}(y, r_x)$, $R_{yy}(y, r_x)$, and $E(y, r_x)$. By contrast, in Fig. 1(c), contours with both positive and negative values are seen for $R_{zz}(y, r_x)$; a direct cascade is observed far from the wall, whereas an inverse cascade is clearly seen near the wall. Because the function $R^>_{\alpha\alpha}(y, r_x)$ corresponds to the GS energy $\langle \bar{u}'^2_\alpha\rangle$, as mentioned above, the flux $\Pi_{S\alpha\alpha}(y, r_x)$ represents energy transfer between the GS and SGS components. Therefore, the energies $\langle \bar{u}'^2_x\rangle$ and $\langle \bar{u}'^2_y\rangle$ are transferred from the GS to the SGS components, whereas the energy $\langle \bar{u}'^2_z\rangle$ is transferred from the SGS to the GS components near the wall. Jiménez [36] discussed the inverse energy cascade from the wall toward the outer flow and examined the energy transfer in the scale and physical (y) spaces simultaneously. By contrast, the present result implies that the inverse energy cascade occurs even at a fixed y location. In general, we can examine the energy flux in the scale space associated with the x-z plane at a fixed y location independently of the wall-normal

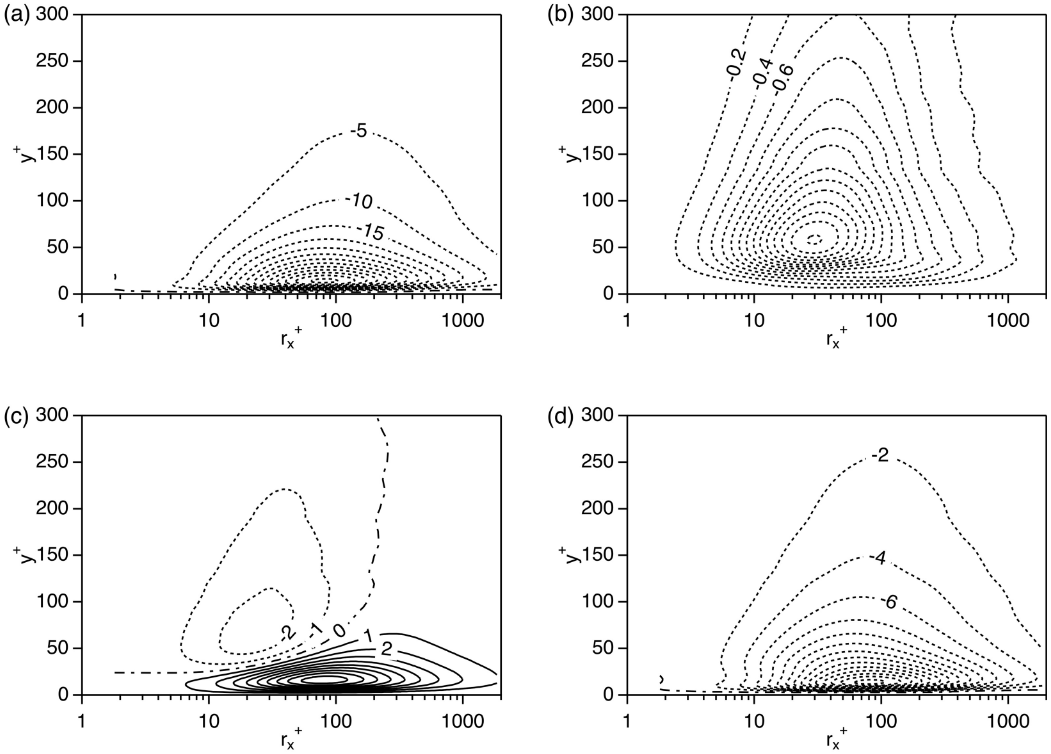

FIG. 1. Contour plots of the energy flux given by Eq. (19) in the r_x-y plane: (a) $\Pi_{Sxx}(y, r_x)$, (b) $\Pi_{Syy}(y, r_x)$, (c) $\Pi_{Szz}(y, r_x)$, and (d) $\Pi_S(y, r_x)$ [$=\Pi_{Sii}(y, r_x)/2$].

flux in the physical space. Similar analysis was carried out using horizontal spectra of energy transport [6]. Here we examine the flux in the r_x space to find an inverse cascade of the spanwise energy component. The peak of $\Pi_{Szz}(y, r_x)$ is located at $y^+ = 16.1$ ($y = 0.0273$) and $r_x^+ = 80.2$ ($r_x = 0.136$) in Fig. 1(c). Its y location corresponds to the buffer layer, where the turbulent kinetic energy has its peak. The length scale $r_x^+ = 80.2$ corresponds to the filter width $\Delta_x^+ = 197$ appearing in Eq. (7). In Fig. 1(c), a contour of zero value shown by the dot-dashed line extends towards the channel center. This indicates that a weak inverse cascade can be seen at $r_x^+ > 200$ even apart from the wall. Because the y location is in the logarithmic layer or in the outer layer, we briefly examine the Reynolds-number dependence of this behavior in the Appendix. A detailed analysis of the inverse cascade in this region is beyond the scope of the present work. In this work we will focus on flow phenomena related to the inverse cascade of $R_{zz}(y, r_x)$ observed at $y^+ = 16.1$ and $r_x^+ = 80.2$, where the energy flux is maximum.

In order to examine the energy transfer near the wall in more detail, we evaluate the transport equation for $R_{\alpha\alpha}(y, r_x)$ given by Eq. (10). Figure 2 shows the premultiplied profiles of terms in the transport equations for $R_{xx}(y, r_x)$, $R_{yy}(y, r_x)$, $R_{zz}(y, r_x)$, and $E(y, r_x)$ as functions of r_x at $y^+ = 16.1$. Terms in the transport equation are multiplied by r_x so that equal areas can represent equal contributions to processes such as production. In Fig. 2(d), the production, dissipation, and transfer terms are dominant in the budget of the turbulent energy $E(y, r_x)$. The production term is positive at large scales, whereas the dissipation term is negative at small scales. The transfer term shows negative values at large scales and positive values at small scales, representing a direct energy cascade from large to small scales. In Fig. 2(a), the overall behavior of the transport equation for $R_{xx}(y, r_x)$ is similar to that for $E(y, r_x)$ in Fig. 2(d), except that the pressure-strain term for the former shows negative values. In Fig. 2(b), the pressure-strain term for $R_{yy}(y, r_x)$, rather than

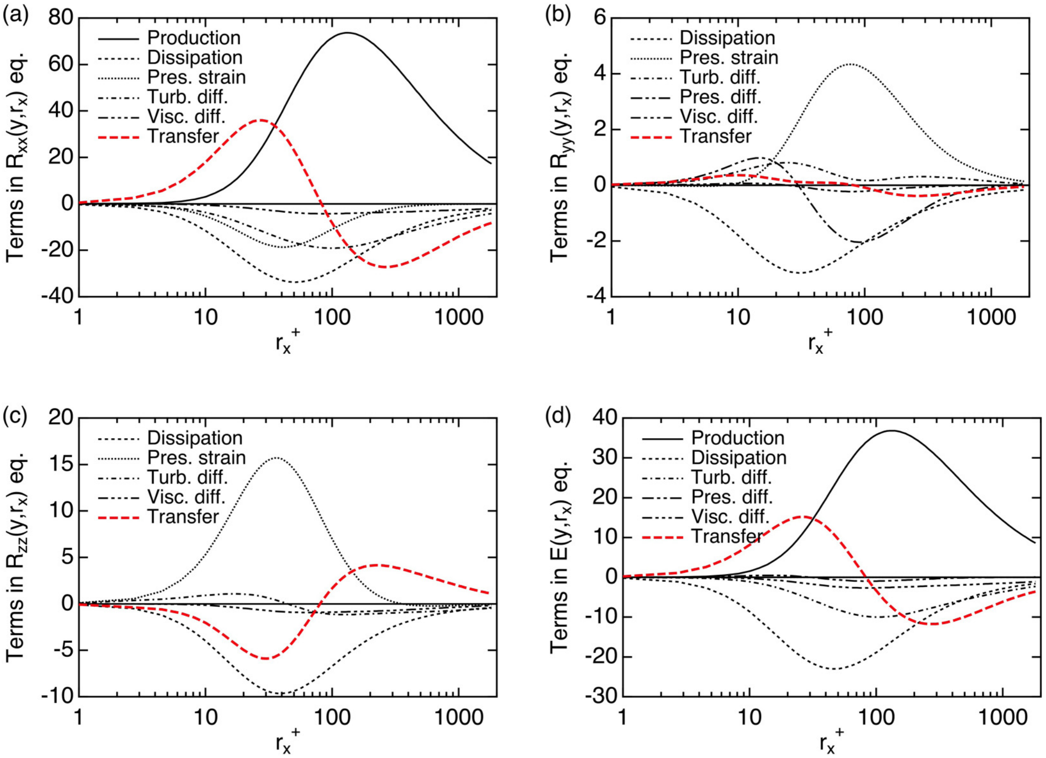

FIG. 2. Terms in the transport equation given by Eq. (10) as functions of r_x at $y^+ = 16.1$ for (a) $R_{xx}(y, r_x)$, (b) $R_{yy}(y, r_x)$, (c) $R_{zz}(y, r_x)$, and (d) $E(y, r_x)$ [$=R_{ii}(y, r_x)/2$].

the production term, shows positive values. The transfer term represents the energy cascade from large to small scales, but its magnitude is small. The pressure-diffusion term contributes mainly to the energy cascade in this case. In Fig. 2(c), by contrast, the transfer term for $R_{zz}(y, r_x)$ exhibits the opposite behavior, that is, an inverse energy cascade from small to large scales. The length scale $r_x^+ = 80.2$ of the peak of the flux $\Pi_{Szz}(y, r_x)$ shown in Fig. 1(c) corresponds to the zero point of the transfer term $T_{zz}(y, r_x)$ in Fig. 2(c). The reason for the inverse cascade is not clear at present, but it must be related to the fact that the peak of the positive pressure-strain term is located at small scales in Fig. 2(c), in contrast to Fig. 2(b).

It is interesting to compare the energy cascade observed here with the self-sustaining process proposed by Waleffe [34]. The self-sustaining process consists of the following three phases. First, streamwise rolls $[0, V(y, z), W(y, z)]$ redistribute the streamwise momentum to create streaks or spanwise fluctuations in the streamwise velocity $U(y) \to U(y, z)$. Second, an instability in $U(y, z)$ causes a three-dimensional disturbance to develop. Third, the nonlinear effect of the three-dimensional disturbance reenergizes the original streamwise rolls. Here the velocity components $U_i(y, z)$ that do not depend on x can be considered as the velocity averaged over a line in the x direction. We can then interpret the process in terms of the energy transfer as follows. The first phase represents energy transfer from the ensemble-averaged velocity $U(y)$ to the line-averaged velocity $U(y, z)$. The second phase represents energy transfer from the line-averaged velocity $U(y, z)$ to the three-dimensional fluctuations. The third phase represents energy transfer from the three-dimensional fluctuations to the line-averaged velocities $V(y, z)$ and $W(y, z)$. Therefore, the first and second phases correspond to the direct energy cascade, whereas the third phase corresponds to the inverse energy cascade. This situation is similar to the present result based on one-dimensional filtering instead of the line average; in Fig. 1, a direct cascade is observed for $R_{xx}(y, r_x)$ and an inverse cascade is observed for $R_{zz}(y, r_x)$, although the cascade of $R_{yy}(y, r_x)$ occurs in the opposite direction to the proposed process. The comparison suggests that the inverse cascade of $R_{zz}(y, r_x)$ shown in Figs. 1(c) and 2(c) can be related to the phase in which the streamwise rolls are reenergized.

III. PRODUCTION TERM OF SGS ENERGY

In this section, in order to understand the mechanism of the inverse cascade of the spanwise energy $R_{zz}(y, r_x)$, we examine the flow structures contributing to this event. The positive flux $\Pi_{Szz}(y, r_x)$ represents the inverse cascade from small to large scales through the length scale r_x. However, we cannot examine the local flow structures by treating only the flux $\Pi_{Szz}(y, r_x)$, because it is an ensemble-averaged quantity and does not have information on the dependence on the x and z locations. As mentioned in Sec. II, this inverse energy cascade corresponds to energy transfer from the SGS component τ_{zz} (where $\tau_{ij} = \overline{u_i u_j} - \bar{u}_i \bar{u}_j$) to the GS component $\bar{u}_z^2$. In general, the energy transfer between the GS component $\bar{u}_\alpha^2$ and the SGS component $\tau_{\alpha\alpha}$ can be expressed as the production term appearing in the transport equation for the SGS energy $\tau_{\alpha\alpha}$, as

$$\bar{P}_{\alpha\alpha} = -2\tau_{\alpha k} \frac{\partial \bar{u}_\alpha}{\partial x_k}, \tag{21}$$

which is defined at each location. The direct (inverse) cascade corresponds to a positive (negative) value of the SGS production term $\bar{P}_{\alpha\alpha}$. In fact, for homogeneous isotropic turbulence, we can obtain the following relationship:

$$\Pi_{S\alpha\alpha} = -\langle \bar{P}_{\alpha\alpha} \rangle. \tag{22}$$

Therefore, in order to examine the flow structures contributing to the inverse cascade of the spanwise energy, we should treat the production term $\bar{P}_{zz}$ defined at each location instead of the ensemble-averaged flux $\Pi_{Szz}(y, r_x)$.

The production term $\bar{P}_{\alpha\alpha}$ can be divided into the isotropic part $P_{I\alpha\alpha}$ and the anisotropic part $P_{A\alpha\alpha}$ as

$$\bar{P}_{\alpha\alpha} = P_{I\alpha\alpha} + P_{A\alpha\alpha}, \quad P_{I\alpha\alpha} = -\frac{2}{3}\tau_{kk} \frac{\partial \bar{u}_\alpha}{\partial x_\alpha}, \quad P_{A\alpha\alpha} = -2\tau^*_{\alpha k} \frac{\partial \bar{u}_\alpha}{\partial x_k}, \tag{23}$$

where $\tau^*_{ij} = \tau_{ij} - \frac{1}{3}\tau_{kk}\delta_{ij}$. The sum of the isotropic part P_{Iii} vanishes because $\nabla \cdot \bar{\mathbf{u}} = 0$. In the transport equation for the GS energy $\bar{u}_\alpha^2$, the corresponding term $-\bar{P}_{\alpha\alpha}$ appears as the dissipation due to the SGS effect. However, it is more appropriate to view the isotropic and anisotropic parts separately; that is, the isotropic part $-P_{I\alpha\alpha}$ represents the energy redistribution among the three GS components $\bar{u}_x^2$, $\bar{u}_y^2$, and $\bar{u}_z^2$, like the pressure term $\bar{p}\partial \bar{u}_\alpha / \partial x_\alpha$ appearing in the $\bar{u}_\alpha^2$ equation, whereas the anisotropic part $-P_{A\alpha\alpha}$ represents the net dissipation into the SGS energy. Therefore, we examine the anisotropic part $P_{A\alpha\alpha}$ rather than $\bar{P}_{\alpha\alpha}$ as the net production term for the SGS energy in this work.

Here we examine the GS velocity field $\bar{u}_i$ and the SGS production term $P_{A\alpha\alpha}$ with $\Delta_x^+ = 197$ ($r_x^+ = 80.2$) in the x-z plane at $y^+ = 16.1$ and $t = 70$. The average $\langle P_{Azz} \rangle_{xz}$ in the x-z plane is -3.14; the anisotropic production actually indicates the inverse cascade. We should note that its local value P_{Azz} can be both positive and negative. In order to examine the behavior of the local value, we evaluate the probability distribution function (PDF) $P(P_{Azz})$ over $N_x \times N_z$ points. The mean value can be expressed as

$$\langle P_{Azz} \rangle_{xz} = \int_{-\infty}^{\infty} dP_{Azz} P_{Azz} P(P_{Azz}). \tag{24}$$

Figure 3(a) shows the PDF of the production term $P(P_{Azz})$. The production term takes large positive and negative values, although the mean value is small. The energy transfer between the GS and SGS components can occur by both direct and inverse cascades. In order to see how large values of P_{Azz}

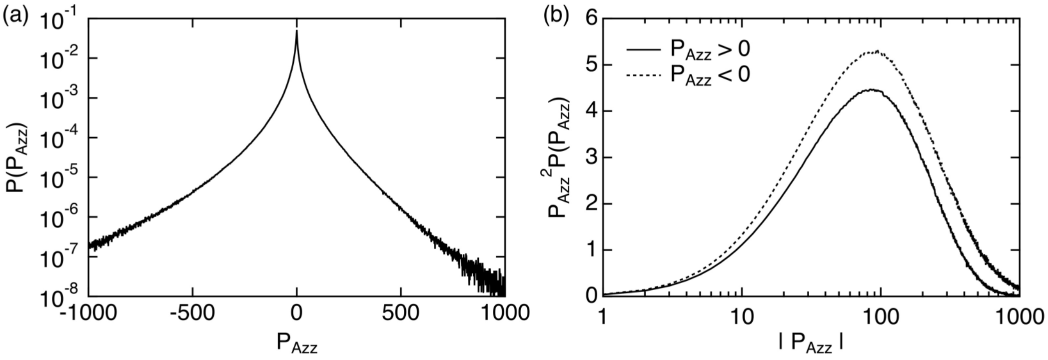

FIG. 3. Profiles of the PDF of SGS production term P_{Azz}: (a) $P(P_{Azz})$ and (b) $P_{Azz}^2 P(P_{Azz})$ as a function of $|P_{Azz}|$.

contribute the most to the average value of $\langle P_{Azz}\rangle_{xz}$, we examine the following quantities by dividing the integral given by Eq. (24) into positive and negative regions:

$$\int_0^{\infty} dP_{Azz}P_{Azz}P(P_{Azz}) = \int_{-\infty}^{\infty} d\ln(P_{Azz})P_{Azz}^2 P(P_{Azz}), \tag{25}$$

$$\int_{-\infty}^{0} dP_{Azz}P_{Azz}P(P_{Azz}) = -\int_{-\infty}^{\infty} d\ln(|P_{Azz}|)P_{Azz}^2 P(P_{Azz}). \tag{26}$$

Figure 3(b) shows the profiles of $P_{Azz}^2 P(P_{Azz})$ as functions of $|P_{Azz}|$ for the positive and negative regions; the premultiplied profiles are shown because it is a semilogarithmic plot. The contribution from the negative region is greater than that from the positive region, so the mean value -3.14 is negative. We can see that the values around $|P_{Azz}| = 100$ contribute the most to the integral in both the positive and negative regions. Therefore, we consider $P_{Azz} = -100$ to be a typical value of the negative production representing the inverse cascade.

In order to examine the vortical structures contributing to the inverse cascade, we plot the isosurfaces of the second invariant of the GS velocity gradient $\bar{q}\,[=-(\partial\bar{u}_i/\partial x_j)(\bar{u}_j/\partial x_i)/2]$. Figure 4 shows the isosurfaces of $\bar{q} = 2000$ (yellow) and those of $P_{Azz} = -100$ (blue) in the domain $0 \leqslant x \leqslant \pi, 0 \leqslant y \leqslant 1$, and $0 \leqslant z \leqslant \pi/2$ $(0 \leqslant x^+ \leqslant 1850, 0 \leqslant y^+ \leqslant 590$, and $0 \leqslant z^+ \leqslant 927)$. The gray plane plotted in Fig. 4(a) represents the x-z plane at $y^+ = 16.1$. We can see many streamwise vortices with sizes approximately as long as Δ_x^+ (=197). The regions where the inverse cascade is

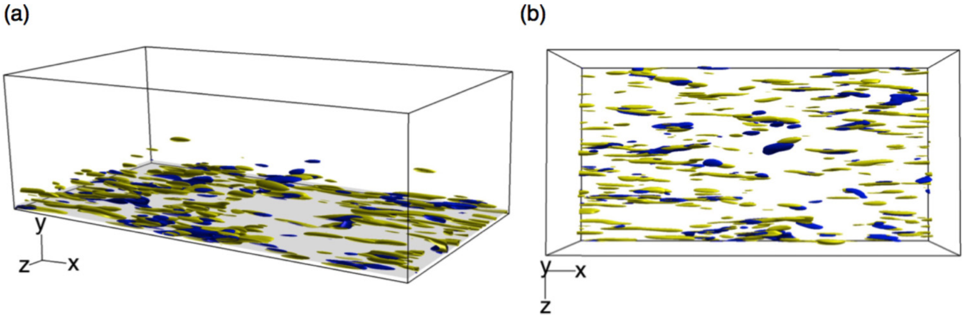

FIG. 4. Isosurfaces of the second invariant $\bar{q} = 2000$ (yellow) and production term $P_{Azz} = -100$ (blue) in the domain $0 \leqslant x \leqslant \pi$, $0 \leqslant y \leqslant 1$, and $0 \leqslant z \leqslant \pi/2$ $(0 \leqslant x^+ \leqslant 1850$, $0 \leqslant y^+ \leqslant 590$, and $0 \leqslant z^+ \leqslant 927)$: (a) perspective view and (b) top view. The gray plane represents the x-z plane at $y^+ = 16.1$.

active are visualized as the isosurfaces of P_{Azz}. These regions tend to be located near some of the streamwise vortices.

The production term P_{Azz} can be further divided into three parts as

$$P_{Azz}\left(=-2\tau^*_{zk}\frac{\partial \bar{u}_z}{\partial x_k}\right) = P_{Azz1} + P_{Azz2} + P_{Azz3}, \tag{27}$$

where

$$P_{Azz1} = -2\tau^*_{zx}\frac{\partial \bar{u}_z}{\partial x}, \quad P_{Azz2} = -2\tau^*_{zy}\frac{\partial \bar{u}_z}{\partial y}, \quad P_{Azz3} = -2\tau^*_{zz}\frac{\partial \bar{u}_z}{\partial z}. \tag{28}$$

Their averaged values at $y^+ = 16.1$ are given by

$$\langle P_{Azz1}\rangle_{xz} = -2.48, \quad \langle P_{Azz2}\rangle_{xz} = -1.38, \quad \langle P_{Azz3}\rangle_{xz} = 0.72, \tag{29}$$

respectively. Therefore, the first and second terms contribute to the inverse cascade and the contribution of the first term is greater. The second term P_{Azz2} involves the velocity gradient $\partial\bar{u}_z/\partial y$, which is part of the streamwise vorticity $\bar{\omega}_x$ [$=(\nabla \times \bar{\mathbf{u}})_x$]. On the other hand, the first term P_{Azz1} involves $\partial\bar{u}_z/\partial x$; this gradient may be related to the gradient of the vorticity in the streamwise direction rather than the streamwise vorticity itself. Because the first term contributes the most, this result suggests that the inverse cascade is closely related to the streamwise variation of the streamwise vortices. In fact, in Fig. 4, some regions of negative production are located near the edge of the streamwise vortices, where the streamwise vorticity increases or decreases in the x direction.

IV. CONDITIONAL AVERAGE OF VELOCITY FIELD

In Sec. III, the isosurfaces of $\bar{q}$ and P_{Azz} plotted in Fig. 4 suggest some relationship between the streamwise vortices and the regions of negative production. However, their relative locations are not necessarily clear because of their variation. In this section, making use of the conditional average of the velocity field, we try to extract typical flow structures contributing to the inverse cascade.

First, we define the conditional average of a quantity f associated with the negative production at the reference point (x, y_0, z) as follows:

$$\langle f\rangle_{C1}(\Delta x, y, \Delta z) = \langle f(x+\Delta x, y, z+\Delta z) | -100.1 < P_{Azz}(x, y_0, z) < -99.9\rangle. \tag{30}$$

The y location of the reference point is set to $y_0^+ = 16.1$. If the value of $P_{Azz}(x, y_0, z)$ is within the above range, then the field of the quantity f around the reference point is added to calculate the averaged field. Because the value of $P_{Azz} = -100$ is a typical one for the negative production, as described in Sec. III, we expect that this conditional average can be used to extract typical flow structures contributing to the inverse cascade.

Figure 5 shows the contours of the conditional averages $\langle\bar{u}_x\rangle_{C1}$, $\langle\bar{u}_y\rangle_{C1}$, $\langle\bar{u}_z\rangle_{C1}$, and $\langle P_{Azz}\rangle_{C1}$ in the x-z plane at $y = y_0$. The dot-dashed lines denote the contours of zero value. The reference point corresponds to $(\Delta x^+, \Delta z^+) = (0, 0)$. The size of the domain $-200 < \Delta x^+ < 200$ in the streamwise direction is approximately twice the filter width Δ_x^+. In Fig. 5(d), the magnitude of $\langle P_{Azz}\rangle_{C1}$ shows a peak at the reference point $(\Delta x^+, \Delta z^+) = (0, 0)$. Negative production is actually seen around this point and it covers a region that is elongated in the streamwise direction. In Fig. 5(b), the wall-normal velocity $\langle\bar{u}_y\rangle_{C1}$ shows large positive values in the upstream region at $\Delta x^+ < 0$ and $\Delta z^+ \simeq 0$, indicating upward flow. The variation of the wall-normal velocity $\langle\bar{u}_y\rangle_{C1}$ in the spanwise direction is directly related to the streamwise vortices because $\bar{\omega}_x = \partial\bar{u}_z/\partial y - \partial\bar{u}_y/\partial z$. The profile shows that the magnitude of the velocity gradient $\partial\langle\bar{u}_y\rangle_{C1}/\partial z$ is large in the upstream regions at $\Delta x^+ < 0$ and $5 < |\Delta z^+| < 30$. The gradient is positive at $\Delta z^+ < 0$ and negative at $\Delta z^+ > 0$; this profile suggests two streamwise vortices rotating in opposite directions. In Fig. 5(a), the streamwise velocity $\langle\bar{u}_x\rangle_{C1}$ is low in the upstream region where $\langle\bar{u}_y\rangle_{C1}$ is positive, so the situation is similar to an ejection event. Along the region of low $\langle\bar{u}_x\rangle_{C1}$ value, two regions of high $\langle\bar{u}_x\rangle_{C1}$ value are seen at $(\Delta x^+, \Delta z^+) = (-100, \pm 50)$. The interval of the two regions is approximately $z^+ = 100$ and

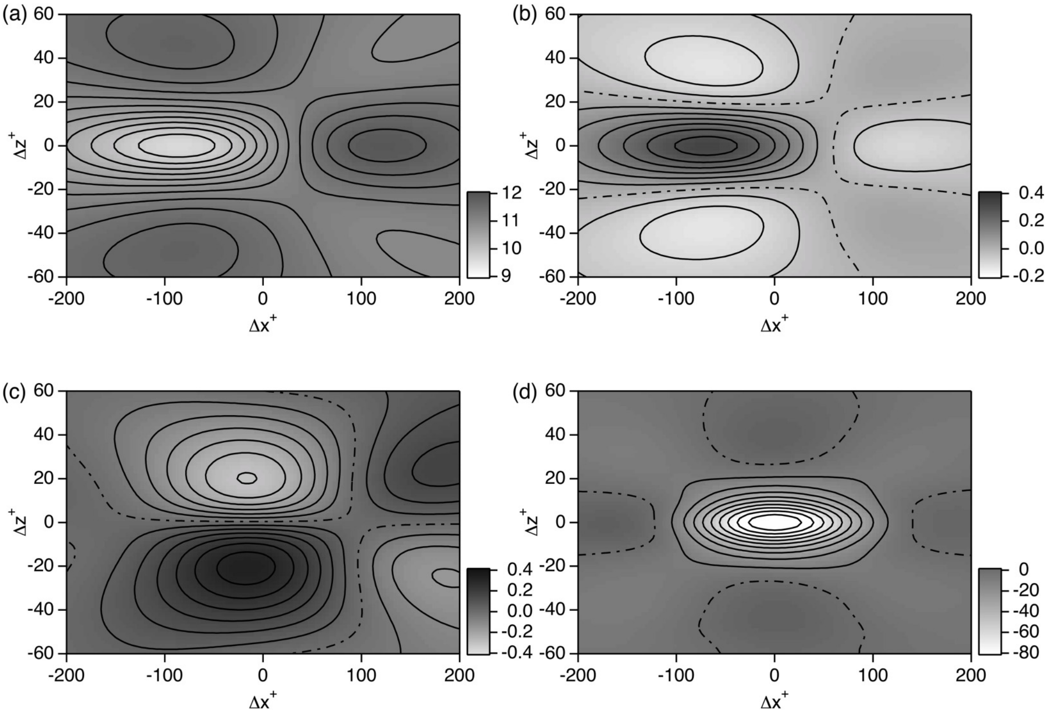

FIG. 5. Contour plots of the conditionally averaged velocity and production term in the x-z plane at $y = y_0$: (a) $\langle \bar{u}_x \rangle_{C1}$, (b) $\langle \bar{u}_y \rangle_{C1}$, (c) $\langle \bar{u}_z \rangle_{C1}$, and (d) $\langle P_{Azz} \rangle_{C1}$.

is associated with the spanwise spacing of near-wall streaks. The velocity gradient $\partial \langle \bar{u}_x \rangle_{C1} / \partial x$ is positive around the reference point, indicating acceleration of the flow in the streamwise direction. In Fig. 5(c), the velocity gradient $\partial \langle \bar{u}_z \rangle_{C1} / \partial z$ is negative around the reference point, indicating contraction in the spanwise direction. Modifying the variable interval time averaging technique, Johansson *et al.* [37] also made conditional sampling for near-wall vortical structures. Figure 6 in [37] is similar to Fig. 5 in the present work; in particular, the distribution of the shear stress $uv - \overline{uv}$ showed negative values around a positive region which is similar to Fig. 5(d). Although detailed

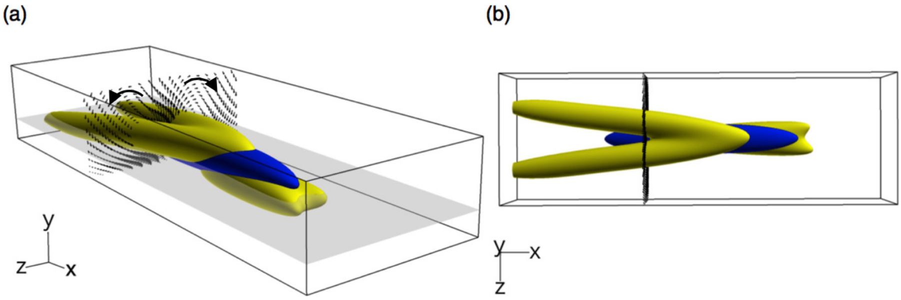

FIG. 6. Isosurfaces of the second invariant $\bar{q}_{C1} = 100$ (yellow) and production term $\langle P_{Azz} \rangle_{C1} = -30$ (blue) in the domain $-0.3 < \Delta x < 0.3$, $0 < y < 0.097$, and $-0.1 < \Delta z < 0.1$ ($-177 < \Delta x^+ < 177$, $0 < y^+ < 57$, and $-59 < \Delta z^+ < 59$): (a) perspective view and (b) top view. The gray plane represents the x-z plane at $y^+ = 16.1$. Velocity vectors in the y-z plane at $\Delta x = -0.09$ are also plotted. Arrows represent the direction of vortex rotation.

methods are different from each other, the results obtained here are closely related to the near-wall shear structure reported by Johansson *et al.* [37].

Next we examine the three-dimensional structure of the conditionally averaged velocity field. The second invariant of the conditionally averaged velocity is given by

$$\bar{q}_{C1} = -\frac{1}{2}\frac{\partial\langle\bar{u}_i\rangle_{C1}}{\partial x_j}\frac{\partial\langle\bar{u}_j\rangle_{C1}}{\partial x_i}. \tag{31}$$

Figure 6 shows the isosurfaces of $\bar{q}_{C1} = 100$ (yellow) and $\langle P_{Azz}\rangle_{C1} = -30$ (blue) in the domain $-0.3 < \Delta x < 0.3, 0 < y < 0.097$, and $-0.1 < \Delta z < 0.1$ ($-177 < \Delta x^+ < 177, 0 < y^+ < 57$, and $-59 < \Delta z^+ < 59$). The gray plane plotted in Fig. 6(a) represents the x-z plane at $y^+ = 16.1$. The isosurfaces of $\bar{q}_{C1}$ show rather complex structures. As discussed above, two streamwise vortices can be seen in the upstream region; they are tilted slightly in the spanwise direction and overlap each other near the reference point. The velocity vectors in the y-z plane are also plotted to show the direction of rotation of the two vortices. In the downstream region at $\Delta x > 0$, we can see another vortical structure. The isosurface of the negative production plotted in blue is located between the upstream and downstream vortices.

The vortical structures shown in Fig. 6 are symmetric about the x-y plane at $\Delta z = 0$. This symmetric profile is obtained because the condition appearing in Eq. (30) is symmetric about $\Delta z = 0$, although the profiles of individual vortices in a snapshot are not necessarily symmetric. It is likely that the two streamwise vortices located upstream in Fig. 6 originally appear independently in a turbulent field and are overlaid by the conditional average. In Sec. III, we found that the velocity gradient $\partial\bar{u}_z/\partial x$ contributes the most to the negative production. However, in Fig. 5(c), its conditional average $\partial\langle\bar{u}_z\rangle_{C1}/\partial x$ vanishes at the reference point because $\langle\bar{u}_z\rangle_{C1} = 0$ along the centerline in the x direction at $\Delta z = 0$. This situation indicates that we cannot extract adequate vortical structure by taking the conditional average defined by Eq. (30), because the important contribution from $\partial\langle\bar{u}_z\rangle_{C1}/\partial x$ is missing.

We thus introduce another conditional average defined as

$$\langle f\rangle_{C2}(\Delta x, y, \Delta z) = \left\langle f(x+\Delta x, y, z+\Delta z) \middle| -100.1 < P_{Azz}(x, y_0, z) < -99.9, \frac{\partial\bar{u}_z}{\partial x}(x, y_0, z) > 0\right\rangle, \tag{32}$$

where the condition $\partial\bar{u}_z/\partial x > 0$ is added to break the symmetry about $\Delta z = 0$. We should note that events with $\partial\bar{u}_z/\partial x > 0$ and those with $\partial\bar{u}_z/\partial x < 0$ occur equally. Here we focus on the events under the former condition. Figure 7 shows the contours of the conditional averages $\langle\bar{u}_x\rangle_{C2}$, $\langle\bar{u}_y\rangle_{C2}$, $\langle\bar{u}_z\rangle_{C2}$, and $\langle P_{Azz}\rangle_{C2}$ in the x-z plane at $y = y_0$. Each figure shows tilted contours, but they are rather simple compared to their counterparts in Fig. 5. In Fig. 7(c), the velocity gradient $\partial\langle\bar{u}_z\rangle_{C2}/\partial x$ clearly shows positive values at the reference point, in contrast to that in Fig. 5(c). In Fig. 7(b), the wall-normal velocity $\langle\bar{u}_y\rangle_{C2}$ shows large positive values in the upstream region at $\Delta x^+ < 0$ and $\Delta z^+ \simeq 0$, like that in Fig. 5(b). However, the symmetry about $\Delta z^+ = 0$ is broken and the velocity gradient $\partial\langle\bar{u}_y\rangle_{C2}/\partial z$ is positive in a wide region around $\Delta z^+ = 0$, suggesting a long streamwise vortex with $\bar{\omega}_x < 0$.

Figure 8 shows the isosurfaces of $\bar{q}_{C2} = 100$ (yellow) and $\langle P_{Azz}\rangle_{C2} = -30$ (blue) in the domain $-0.37 < \Delta x < 0.37$, $0 < y < 0.097$, and $-0.1 < \Delta z < 0.1$ ($-218 < \Delta x^+ < 218$, $0 < y^+ < 57$, and $-59 < \Delta z^+ < 59$), where $\bar{q}_{C2}$ is defined by an equation similar to Eq. (31). The gray plane plotted in Fig. 8(a) represents the x-z plane at $y^+ = 16.1$. We should note that Fig. 7 corresponds not to the top view but to the bottom view of the three-dimensional plot in Fig. 8. We can clearly see two streamwise vortices in Fig. 8. The long vortex is slightly tilted in the $+z$ direction and is accompanied by a short vortex in the upstream region. The two vortices rotate in opposite directions, as shown by the velocity vectors in the y-z plane. These profiles in Fig. 8 are simple compared to those plotted in Fig. 6 and seem to be more realistic as typical vortical structures. Figure 8 reminds us of a series of slightly tilted streamwise vortices with alternate signs of vorticity near the wall investigated by previous works [38,39]. In fact, in Fig. 4 we can see that some streamwise vortices

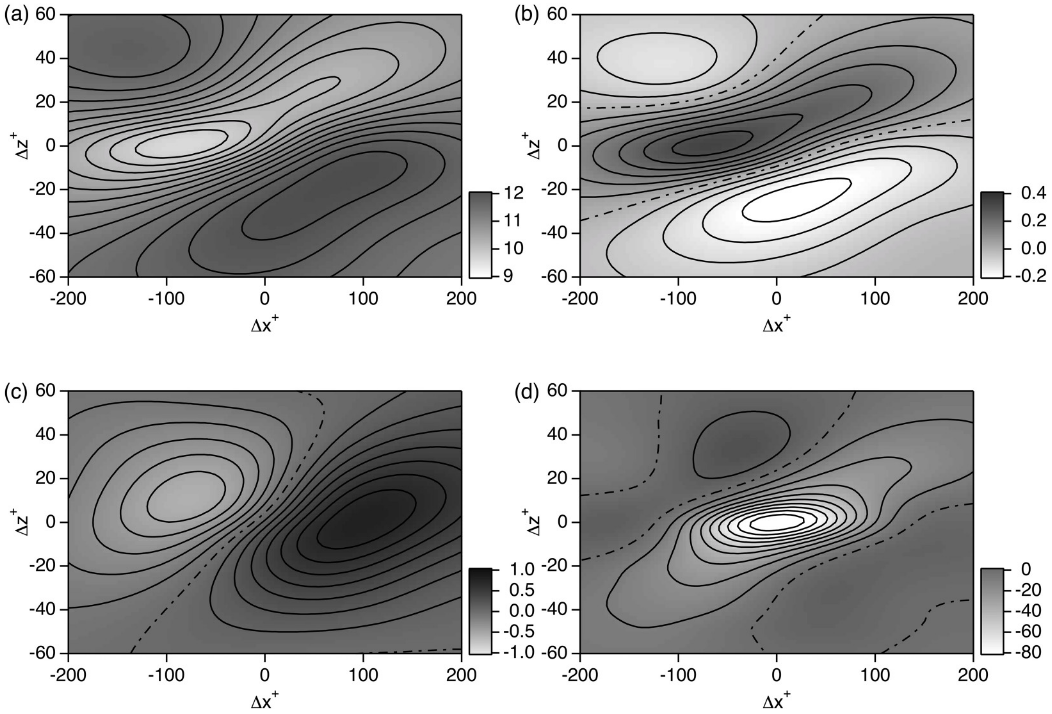

FIG. 7. Contour plots of the conditionally averaged velocity and production term in the x-z plane at $y = y_0$: (a) $\langle \bar{u}_x \rangle_{C2}$, (b) $\langle \bar{u}_y \rangle_{C2}$, (c) $\langle \bar{u}_z \rangle_{C2}$, and (d) $\langle P_{Azz} \rangle_{C2}$.

tilted in the $+z$ direction are aligned with others tilted in the $-z$ direction. We believe that the profiles plotted in Fig. 8 reflect such a series of streamwise vortices near the wall. The upstream vortex shown in Fig. 8 is short and weak compared to the long vortex; the magnitude of the vorticity must be weakened in the process of taking the conditional average, although individual upstream vortices in a snapshot should be as strong as the long one.

The isosurface of $\langle P_{Azz} \rangle_{C2}$ is located between the two vortices, suggesting that the inverse cascade is driven by the interaction of the two vortices. Because the isosurface appears mainly along the

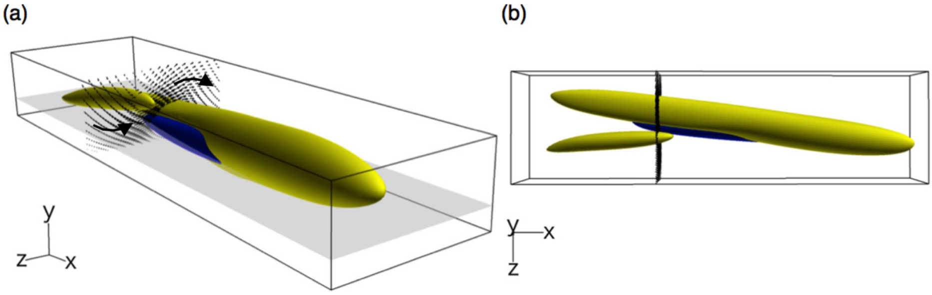

FIG. 8. Isosurfaces of the second invariant $\bar{q}_{C2} = 100$ (yellow) and production term $\langle P_{Azz} \rangle_{C2} = -30$ (blue) in the domain $-0.37 < \Delta x < 0.37$, $0 < y < 0.097$, and $-0.1 < \Delta z < 0.1$ ($-218 < \Delta x^+ < 218$, $0 < y^+ < 57$, and $-59 < \Delta z^+ < 59$): (a) perspective view and (b) top view. The gray plane represents the x-z plane at $y^+ = 16.1$. Velocity vectors in the y-z plane at $\Delta x = -0.11$ are also plotted. Arrows represent the direction of vortex rotation.

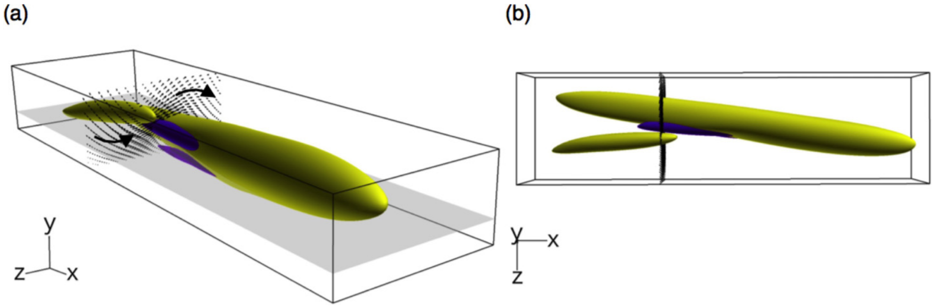

FIG. 9. Isosurfaces of the second invariant $\bar{q}_{C2} = 100$ (yellow) and enstrophy production term $\langle P_{\omega xx}\rangle_{C2} = -250\,000$ (violet) in the domain $-0.37 < \Delta x < 0.37$, $0 < y < 0.097$, and $-0.1 < \Delta z < 0.1$ ($-218 < \Delta x^+ < 218$, $0 < y^+ < 57$, and $-59 < \Delta z^+ < 59$): (a) perspective view and (b) top view. The gray plane represents the x-z plane at $y^+ = 16.1$. Velocity vectors in the y-z plane at $\Delta x = -0.11$ are also plotted. Arrows represent the direction of vortex rotation.

long vortex, the negative production should represent enhancement of the GS velocity of the long vortex, that is, an increase in the rotation of the long vortex. It does not mean that the short upstream vortex directly drives the rotation of the long vortex; this phenomenon would be expressed as energy transfer between the GS velocities because the short vortex is also based on the GS velocity. A negative value of $\langle P_{Azz}\rangle_{C2}$ represents energy transfer from the SGS to the GS components. We should consider that the SGS motion not plotted in the figure enhances the GS velocity of the long vortex under the influence of the short vortex. In typical situations, the SGS motion acts as the effective viscosity for the GS velocity; this means that the GS vorticity is usually diffused and weakened by the SGS effect. However, in the regions of negative SGS production, the GS vorticity is not diffused but enhanced by the SGS motion via the upstream vortex.

In order to check whether the negative production actually indicates an increase in the rotation of the long vortex, we examine the transport equation for the GS vorticity $\bar{\omega}_x$. From the Navier-Stokes equation for the GS velocity, we can obtain the equation for the streamwise component of the GS enstrophy $\bar{\omega}_x^2$ as

$$\frac{\partial}{\partial t}\bar{\omega}_x^2 = -P_{\omega xx} + \cdots, \quad P_{\omega xx} = -2\varepsilon_{xjk}\frac{\partial \tau_{km}^*}{\partial x_j}\frac{\partial \bar{\omega}_x}{\partial x_m}, \tag{33}$$

where only the terms describing the interaction between the GS and SGS components are written on the right-hand side for simplicity. The term $P_{\omega xx}$ is part of the production term in the SGS enstrophy equation. A negative value of $P_{\omega xx}$ represents enhancement of the GS vorticity $\bar{\omega}_x$, that is, an increase in the rotation of the GS vortex. Figure 9 shows the isosurfaces of $\bar{q}_{C2} = 100$ (yellow) and $\langle P_{\omega xx}\rangle_{C2} = -250\,000$ (violet) in the domain $-0.37 < \Delta x < 0.37$, $0 < y < 0.097$, and $-0.1 < \Delta z < 0.1$ ($-218 < \Delta x^+ < 218$, $0 < y^+ < 57$, and $-59 < \Delta z^+ < 59$). The isosurfaces of $\bar{q}_{C2}$ are the same as those plotted in Fig. 8. The isosurfaces of $\langle P_{\omega xx}\rangle_{C2}$ are attached to the long vortex and located near those of $\langle P_{Azz}\rangle_{C2}$ plotted in Fig. 8. These profiles confirm that the inverse cascade represented by $\langle P_{Azz}\rangle_{C2}$ is directly related to the increase in the rotation of the long vortex.

In Sec. II we mentioned the self-sustaining process proposed by Waleffe [34] in terms of the energy transfer. The third phase of the process can be considered as the inverse cascade from the three-dimensional fluctuations to the line-averaged velocities $V(y, z)$ and $W(y, z)$. The line-averaged velocity and three-dimensional fluctuations correspond to the GS and SGS velocities in our analysis, respectively. The region of negative production attached to the long vortex plotted in Fig. 8 shows that the GS velocity field of the long vortex is enhanced by the SGS motion. Moreover, the region of negative enstrophy production plotted in Fig. 9 confirms that the SGS effect increases the rotation of the long vortex; that is, the effect of the three-dimensional fluctuations reenergizes the streamwise rolls. Therefore, the results obtained in this section indicate that the third phase of the process is actually observed for the GS velocity field with the streamwise filtering used here. The near-wall vortical structures are expected to be described adequately in wall units whereas some statistics may depend on the Reynolds number in a different manner. Although a systematic survey of the Reynolds-number dependence is beyond the scope of this paper, a preliminary analysis of the similarity and dependence is made in the Appendix.

V. CONCLUSION

The energy transfer in scale space was examined using the DNS data of turbulent channel flow. The energy flux term was evaluated for the normal Reynolds stresses and the turbulent energy. A direct cascade of the streamwise and wall-normal components of the turbulent energy was seen, whereas an inverse cascade of the spanwise component was observed near the wall. In order to understand the flow structures related to the inverse cascade, we focused on the production term of the SGS energy instead of the energy flux term in scale space. The isosurfaces of the second invariant of the GS velocity gradient and those of the SGS production showed that the regions of negative production were located near the streamwise vortices. However, the relative locations of the streamwise vortices and negative production regions were not necessarily clear because of their variation.

In order to extract the typical flow structures contributing to the inverse cascade, we evaluated the conditional average of the velocity field associated with negative production of the SGS energy. The observed structure was rather complex: Two streamwise vortices overlapped near the reference point and the region of negative production appeared between these vortices and the small downstream vortices. In order to break the symmetry in the spanwise direction and obtain simple vortical structures, we added another condition for taking the average. As a result, a long streamwise vortex around the reference point and a short one in the upstream region were observed. These vortices remind us of a series of slightly tilted streamwise vortices with alternate signs of vorticity near the wall. The isosurface of the negative production suggests that the GS velocity of the long vortex is enhanced by the SGS motion under the influence of the short upstream vortex. We further examined the enstrophy equation to confirm that the SGS effect increases the rotation of the long streamwise vortex. We believe that this analysis of the conditional average provides insight into the self-sustaining process of the streamwise vortices and the generation mechanism of the turbulent energy near the wall.

ACKNOWLEDGMENT

This work was supported by JSPS KAKENHI Grant No. JP17K06143.

APPENDIX: REYNOLDS-NUMBER DEPENDENCE OF NEAR-WALL STRUCTURES

It is expected that the energy transport and the vortical structures near the wall can be described adequately in wall units. At the same time, large-scale structures in the outer layer may affect the near-wall structures; their statistics may depend on the Reynolds number in a different manner. A systematic survey of the Reynolds number dependence needs to be done in future work. Here we show preliminary results of the Reynolds-number similarity and dependence. In addition to the DNS data at $\mathrm{Re}_\tau = 590$, we carried out a DNS of channel flow at $\mathrm{Re}_\tau = 395$ for comparison.

First, we examine the inverse energy cascade observed in Fig. 1(c). Figure 10 shows the contours of the energy flux $\Pi_{Szz}(y, r_x)$ for $\mathrm{Re}_\tau = 395$. The contours are very similar to those in Fig. 1(c) for $\mathrm{Re}_\tau = 590$. The peak of the flux is located at $y^+ = 16.1$ and $r_x^+ = 78.6$; the values are nearly the same as those in Fig. 1(c). Therefore, the location and size of the inverse energy cascade near the wall can be described adequately in wall units. As already mentioned in Sec. II, a contour of zero value extending towards the channel center suggested a weak inverse cascade in the region apart

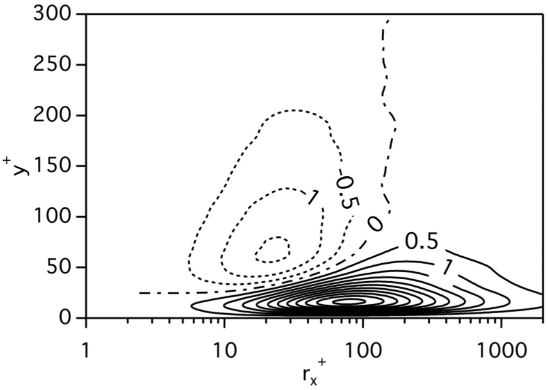

FIG. 10. Contour plots of the energy flux $\Pi_{Szz}(y, r_x)$ given by Eq. (19) in the r_x-y plane for $\mathrm{Re}_\tau = 395$.

from the wall. The behavior of such regions may depend on the Reynolds number in a different manner. In fact, the zero-value contour is located at $r_x^+ = 200$ in Fig. 1(c) whereas it is located at $r_x^+ = 150$ in Fig. 10.

Next we examine the vortical structures in the near-wall region. The size of the isosurfaces plotted in Figs. 6 and 8 depends on their threshold values; the comparison of results between the different Reynolds numbers is not necessarily easy. Here we examine the contour plots of the velocity in the x-z plane shown in Figs. 5 and 7. Figure 11 shows the contours of the conditional averages $\langle \bar{u}_x \rangle_{C1}$ and $\langle \bar{u}_y \rangle_{C1}$ given by Eq. (30) in the x-z plane for $\mathrm{Re}_\tau = 395$. Figures 11(a) and 11(b) correspond to Figs. 5(a) and 5(b), respectively, for $\mathrm{Re}_\tau = 590$. The contours are very similar between the two figures. The contours of the conditional averages $\langle \bar{u}_x \rangle_{C2}$ and $\langle \bar{u}_y \rangle_{C2}$ given by Eq. (32) are also very similar between $\mathrm{Re}_\tau = 590$ and 395 as shown in Figs. 7 and 12. Therefore, near-wall structures observed in the present work are described adequately in wall units.

Waleffe and Kim [40] estimated that streamwise roles $[0, V(y,z), W(y,z)]$ exhibit a Re^{-1} dependence whereas streaks $U(y,z)$ remain essentially Re independent; that is, the former is described in wall units and the latter is as large as the outer layer. Abe *et al.* [41] examined the Reynolds-number dependence of turbulence statistics and structures in a streamwise minimal unit of channel flow. They observed that large-scale structures are essentially two dimensional at large Reynolds number and confirmed the expectation of Waleffe and Kim [40]. In the present work it is confirmed that streamwise roles are described in wall units in Figs. 11(b) and 12(b). However, the streamwise velocity in Figs. 11(a) and 12(a) are also described in wall units and large-scale

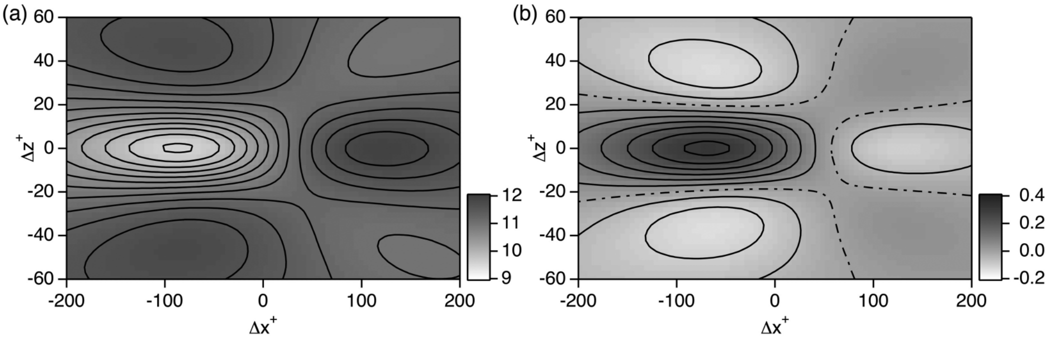

FIG. 11. Contour plots of the conditionally averaged velocity in the x-z plane at $y = y_0$ for $\mathrm{Re}_\tau = 395$: (a) $\langle \bar{u}_x \rangle_{C1}$ and (b) $\langle \bar{u}_y \rangle_{C1}$.

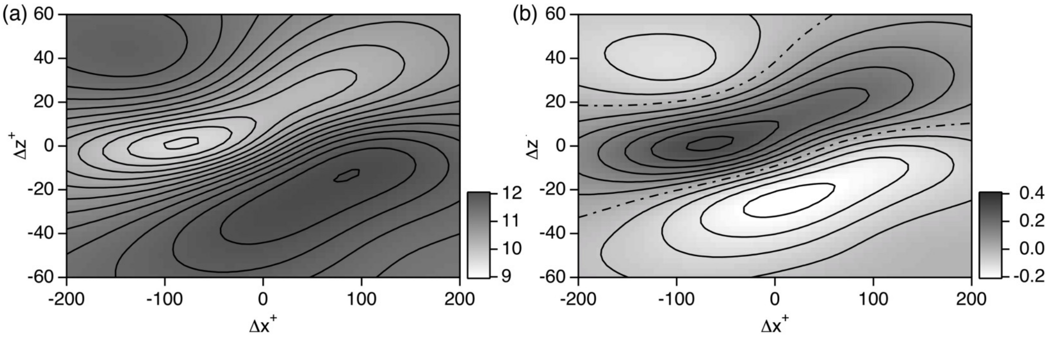

FIG. 12. Contour plots of the conditionally averaged velocity in the x-z plane at $y = y_0$ for $\mathrm{Re}_\tau = 395$: (a) $\langle \bar{u}_x \rangle_{C2}$ and (b) $\langle \bar{u}_y \rangle_{C2}$.

structures of streaks are not observed. This is partly because of the choice of the conditional average; the SGS production should be closely related to near-wall structures. It must be interesting to choose other conditions to see if large-scale structures are extracted or not.

---

[1] U. Frisch, *Turbulence* (Cambridge University Press, Cambridge, 1995).
[2] S. B. Pope, *Turbulent Flows* (Cambridge University Press, Cambridge, 2000).
[3] J. A. Domaradzki, W. Liu, C. Härtel, and L. Kleiser, Energy transfer in numerically simulated wall-bounded turbulent flows, Phys. Fluids **6**, 1583 (1994).
[4] D. C. Dunn and J. F. Morrison, Anisotropy and energy flux in wall turbulence, J. Fluid Mech. **491**, 353 (2003).
[5] I. A. Bolotnov, R. T. Lahey Jr., D. A. Drew, K. E. Jansen, and A. A. Oberai, Spectral analysis of turbulence based on the DNS of a channel flow, Comput. Fluids **39**, 640 (2010).
[6] Y. Mizuno, Spectra of energy transport in turbulent channel flows for moderate Reynolds numbers, J. Fluid Mech. **805**, 171 (2016).
[7] M. Lee and R. D. Moser, Spectral analysis of the budget equation in turbulent channel flows at high Reynolds number, J. Fluid Mech. **860**, 886 (2019).
[8] L. Danaila, F. Anselmet, T. Zhou, and R. A. Antonia, Turbulent energy scale budget equations in a fully developed channel flow, J. Fluid Mech. **430**, 87 (2001).
[9] R. J. Hill, Exact second-order structure-function relationships, J. Fluid Mech. **468**, 317 (2002).
[10] N. Marati, C. M. Casciola, and R. Piva, Energy cascade and spatial fluxes in wall turbulence, J. Fluid Mech. **521**, 191 (2004).
[11] P. A. Davidson, *Turbulence* (Oxford University Press, Oxford, 2004).
[12] L. Danaila, J. F. Krawczynski, F. Thiesset, and B. Renou, Yaglom-like equation in axisymmetric anisotropic turbulence, Physica D **241**, 216 (2012).
[13] A. Cimarelli, E. De Angelis, and C. M. Casciola, Paths of energy in turbulent channel flows, J. Fluid Mech. **715**, 436 (2013).
[14] F. Hamba, Turbulent energy density and its transport equation in scale space, Phys. Fluids **27**, 085108 (2015).
[15] A. Cimarelli, E. De Angelis, J. Jiménez, and C. M. Casciola, Cascades and wall-normal fluxes in turbulent channel flows, J. Fluid Mech. **796**, 417 (2016).
[16] J.-P. Mollicone, F. Battista, P. Gualtieri, and C. M. Casciola, Turbulence dynamics in separated flows: The generalised Kolmogorov equation for inhomogeneous anisotropic conditions, J. Fluid Mech. **841**, 1012 (2018).

[17] F. Hamba, Turbulent energy density in scale space for inhomogeneous turbulence, J. Fluid Mech. **842**, 532 (2018).

[18] S. K. Robinson, Coherent motion in the turbulent boundary layer, Annu. Rev. Fluid Mech. **23**, 601 (1991).

[19] K. C. Kim and R. J. Adrian, Very large-scale motion in the outer layer, Phys. Fluids **11**, 417 (1999).

[20] R. J. Adrian, C. D. Meinhart, and C. D. Tomkins, Vortex organization in the outer region of the turbulent boundary layer, J. Fluid Mech. **422**, 1 (2000).

[21] H. Abe, H. Kawamura, and H. Choi, Very large-scale structures and their effects on the wall shear-stress fluctuations in a turbulent channel flow up to $Re_\tau = 640$, ASME J. Fluids Eng. **126**, 835 (2004).

[22] R. J. Adrian, Hairpin vortex organization in wall turbulence, Phys. Fluids **19**, 041301 (2007).

[23] A. J. Smits, B. J. McKeon, and I. Marusic, High-Reynolds number wall turbulence, Annu. Rev. Fluid Mech. **43**, 353 (2011).

[24] J. Jiménez, Cascades in wall-bounded turbulence, Annu. Rev. Fluid Mech. **44**, 27 (2012).

[25] J. Ahn, J. H. Lee, J. Lee, J.-H. Kang, and H. J. Sung, Direct numerical simulation of a 30R long turbulent pipe flow at $Re_\tau = 3008$, Phys. Fluids **27**, 065110 (2015).

[26] J. Jiménez, Coherent structures in wall-bounded turbulence, J. Fluid Mech. **842**, P1 (2018).

[27] I. Marusic and J. P. Monty, Attached eddy model of wall turbulence, Annu. Rev. Fluid Mech. **51**, 49 (2019).

[28] N. Hutchins and I. Marusic, Evidence of very long meandering features in the logarithmic region of turbulent boundary layers, J. Fluid Mech. **579**, 1 (2007).

[29] J. Zhou, R. J. Adrian, S. Balachandar, and T. M. Kendall, Mechanisms for generating coherent packets of hairpin vortices in channel flow, J. Fluid Mech. **387**, 353 (1999).

[30] J. Hwang and H. J. Sung, Influence of large-scale motions on the frictional drag in a turbulent boundary layer, J. Fluid Mech. **829**, 751 (2017).

[31] C. M. de Silva, Kevin, R. Baidya, N. Hutchins, and I. Marusic, Large coherence of spanwise velocity in turbulent boundary layers, J. Fluid Mech. **847**, 161 (2018).

[32] R. J. Adrian and Z.-C. Liu, Observation of vortex packets in direct numerical simulation of fully turbulent channel flow, J. Visual. **5**, 9 (2002).

[33] B. J. McKeon, The engine behind (wall) turbulence: Perspectives on scale interactions, J. Fluid Mech. **817**, P1 (2017).

[34] F. Waleffe, On a self-sustaining process in shear flows, Phys. Fluids **9**, 883 (1997).

[35] Y. Motoori and S. Goto, Generation mechanism of a hierarchy of vortices in a turbulent boundary layer, J. Fluid Mech. **865**, 1085 (2019).

[36] J. Jiménez, The physics of wall turbulence, Physica A **263**, 252 (1999).

[37] A. V. Johansson, P. H. Alfredsson, and J. Kim, Evolution and dynamics of shear-layer structures in near-wall turbulence, J. Fluid Mech. **224**, 579 (1991).

[38] J. Kim and F. Hussain, Propagation velocity of perturbations in turbulent channel flow, Phys. Fluids A **5**, 695 (1993).

[39] Y. Miyake, R. Ushiro, and T. Morikawa, On regeneration of quasi-streamwise vortices of near wall-turbulence, Trans. Jpn. Soc. Mech. Eng. B **61**, 1272 (1995).

[40] F. Waleffe and J. Kim, in *Self-Sustaining Mechanisms of Wall-Bounded Turbulence*, edited by R. L. Panton (Computational Mechanics, Southampton, 1997), p. 309.

[41] H. Abe, R. A. Antonia, and S. Toh, Large-scale structures in a turbulent channel flow with a minimal streamwise flow unit, J. Fluid Mech. **850**, 733 (2018).